A soft-robotic end-effector for independently actuating endoscopic catheters

Ashwin K. P.
Graduate Student, Department of Mechanical Engineering
Indian Institute of Science
Bangalore 560 012, India
Email: ashwinkp@iisc.ac.in

Ashitava Ghosal *
Professor, Department of Mechanical Engineering
Indian Institute of Science
Bangalore 560 012, India
Email: asitava@iisc.ac.in
Tel. +91 80 2293 2956

Abstract
This paper deals with the design, development, modeling and experimental validation of a prototype endoscopic attachment that can be actuated independently by soft actuators to position an endoscopic catheter tip to a desired location. The soft actuators are miniaturized pneumatic artificial muscles (MPAMs) and by applying 137 kPa–827 kPa pressure to one or more MPAMs, the tip of the endoscopic catheter can be positioned in an approximately hemispherical region of 45 mm radius. An optimization-based forward kinematic model to predict the profile of the actuated end-effector is developed. Experiments conducted on the prototype show that the kinematics model can predict the deformation profile of the end-effector with a maximum error of 2 mm. An inverse kinematics model to estimate the pressure required in the MPAMs to position the tip of the catheter at a specified point is also developed. The pressures in the MPAMs are controlled using an ATmel ATMega 2560 micro-controller with the inputs generated with a thumb-stick to show that real-time actuation is possible. Finally, ex-vivo experiments were conducted to show that the developed prototype end-effector can be successfully used to independently actuate endoscopic catheters.

1 Introduction

An endoscope is a flexible tube which is inserted into a patient's gastrointestinal (GI) tract from the mouth with the primary objective of real-time inspection and diagnosis. The typical endoscope is approximately 1.5 m long and about 12 mm in diameter and once in the desired region of the GI tract, the distal end which is inside the body can be rotated by the clinician/surgeon about two axis (using two rotary knobs) to image the region of the GI tract. To image the region, at the distal end there is a camera with an illumination system. There are also openings for pumping air and water to remove obstacles such as food during the motion of the endoscope along the GI tract. Most of the modern endoscopes are also equipped with one or two channels through which medical instruments (catheters) can be pushed by a surgeon, from the holding (proximal) end, till its tool tip protrudes from the distal end of the endoscope. Although the endoscope and the camera optics can be moved in two directions, endoscopes in general do not have a provision to actuate the catheter independent of the camera. A few automated endoscopic platforms have the ability to actuate the inserted catheter with end-effector (such as a gripper) for performing surgery [1,2]. Positioning of the end-effector is typically achieved using a cable driven continuum robot [3,4]. Though it is possible to achieve precise control using cable actuation ([4,5]), tissue damages or perforation could occur, if the end-effector is not properly manipulated. This is because the device becomes a stiff structure in the actuation plane when deployed [6]. Hence, there has been considerable focus in developing devices which are soft and flexible for applications involving human interactions [7–9].

Soft actuators such as pneumatic artificial muscles (PAMs), also called McKibben actuators, are more suitable for such applications since the actuators are compliant/flexible even in its actuated state and the perforation of tissues due to incorrect actuation could be avoided [10]. The first PAM was invented by Gaylord [11] and consisted of an inflatable bladder braided on the lateral outer surface with a mesh of flexible but inextensible fibers. One end of the PAM is sealed and air is pumped into the bladder from the

*Corresponding Author

other end. If the braiding angle is less than 54.7°, the bladder contracts along its length [12] and can also apply a force. This contraction behavior is similar to muscles thus giving rise to the term "artificial muscles". For a while PAMs and miniaturized versions of PAMs (MPAMs) were not used extensively in robotics possibly due to their inherent nonlinear force-displacement characteristics and the resultant difficulty in control and, more likely, due to easy availability of very good electric motors. In the recent past, PAMs and MPAMs are being suggested for medical robotics since they have high load carrying capacity, their stiffness can be controlled by the internal pressure, have low weight, and are less expensive to manufacture (see also [13–18]). Due to these reasons, they also perform better when compared to other soft actuators such as shape memory alloys(SMA), electro-active polymers, dielectric elastomers etc. [19–21]. The advancement in control strategies have made these actuators popular in bio-inspired and medical robotics (see [19, 22–28]).

In this work, we present the design and analysis of an MPAM actuated end-effector, which can independently deflect an endoscopic catheter up to 25 mm in different directions upon application of pressurized air ranging from 137 kPa–827 kPa. The proposed design of the end-effector is detailed in section 2. A prototype about 50 mm long and 8 mm in diameter has been fabricated. The MPAMs used in the design is characterized in section 3 where we also present an improved mathematical model for predicting pressure-deformation relationship in MPAMs. In section 4, an optimization-based forward kinematics model of the end-effector, to predict the profile of the actuated end-effector, is derived. An inverse-kinematics model to estimate the pressure required to position the catheter at a particular point in the end-effector workspace is detailed in section 5. A method to actuate the end-effector in real-time by integrating the same with a thumb-stick is also discussed in this section. In section 5.3, results from experiments conducted using end-effector are presented and discussed. Finally, conclusions of the work are presented in section 6.

2 Design of end-effector

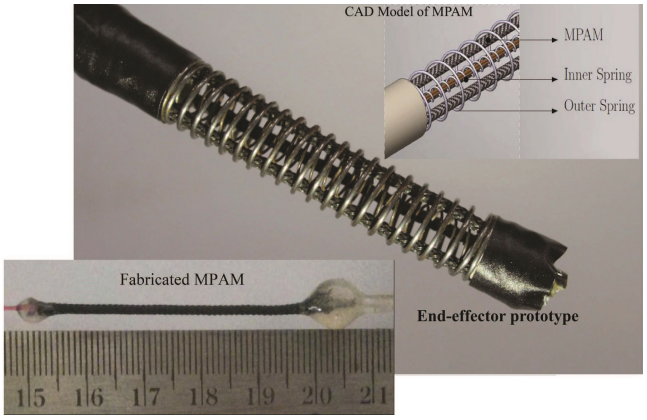

Fig. 1: End-effector prototype and MPAM assembly

As mentioned earlier, at the free end of an actual endoscope, there would be a camera together with a lighting system, openings for spraying water and air and a channel through which an end-effector can be pushed by the surgeon. In this work, we focus on the end-effector assembly with endoscopic tool/catheter attached to the tip which can be deflected independent of the camera assembly. The conceptual design of the end-effector assembly was originally presented in [29].

Fig. 1 shows the fabricated end-effector, together with the arrangement of the three MPAMs and the fabricated MPAM. Considering the size of an endoscope, the end-effector length is chosen to be 50 mm and the outer diameter as 8 mm – to accommodate other accessories at the tip of the endoscope. As shown in the bottom left inset, the fabricated MPAM is about 45 mm long and 1.2 mm outer diameter. The inner tube is made of platinum cured silicone used in medical applications. We used 30 strands of nylon fibers to braid the outer surface of the tube with each strand 50 micrometers in diameter. As shown in the inset CAD model, it consists of two concentric helical springs of 8 mm and 3 mm diameter with 0.5 mm thickness. The three MPAMs are placed parallel to the axis of the springs in the space between the inner and outer springs. The three MPAMs are placed approximately 120 degrees apart and are capped at the ends along with the springs using holders – the outer springs need to be covered with a bio-compatible flexible layer so that insides will not be exposed to GI tract fluids in an actual device. The MPAMs can be energized using pressurized air applied through tubes connected to a reservoir. The inner spring acts as a channel for passing the catheter. It may be noted that most of the commonly used catheters have a design where the tool at the tip is actuated by a set of cables which run through a closely wound coil and protective sheath. If the working end of the catheter/instrument is fixed at the tip of end-effector, leaving the inner spring of end-effector to act as a conduit for actuation cables, the diameter of the inner spring, and consequently the end-effector diameter can be reduced to about 6 mm. Both the springs have low axial as well as transverse stiffness with the axial stiffness of inner spring slightly higher compared to the outer spring. This enables the tip of inner spring to act as a fulcrum whenever the MPAM contracts, facilitating its deflection. Due to the arrangement and contraction in the MPAMs, by actuating two MPAMs at a time, the tip of end-effector can be positioned in a section of a hemisphere of radius 45 mm.

Fig. 2 shows the hardware components used to actuate an MPAM. A pneumatic compressor of maximum output pressure 1034 kPa (150 psi) is connected to a 1 liter air reservoir which is used to deliver high pressure air to the MPAM. A pressure regulating circuit operates the compressor when the value of pressure in reservoir falls below certain threshold thereby maintaining availability of 827 kPa (120 psi) pressure at all times. The volume of air in the MPAM is about 30 mm^3 and this small volume is not expected to result in safety issue in case of leakage. In addition, the flow control valve limits the volume flow rate of air into the MPAM to avoid sudden bleeding of compressed air from the reser-

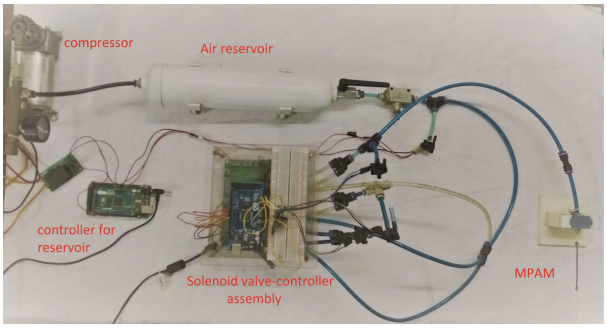

Fig. 2: Experimental set-up for applying pressure to MPAMs. Six solenoid valves are used to control pressure in three MPAMs

voir to the MPAM. Two proportional valves are used to control pressure inside an air muscle – one for pressurizing the MPAM and the other for bleeding. A Honeywell pressure transducer (with range of 0 to 1034 kPa) is connected in series with MPAM to measure the inner pressure. An ATmel ATMega2560 micro-controller board interfaced with MATLAB [30] controls the proportional valves through a current driver circuit to maintain desired value of pressure inside the MPAM. We used a simple PID controller (see [14] for details) to control the pressure inside MPAMs. To measure the tip displacement of a single MPAM and for the entire end-effector, high resolution cameras and image processing were used. The maximum error due to the image processing was found to be about 0.2 mm.

3 Mathematical modeling of MPAM

In a recent work [20], the authors have presented a detailed review of existing mathematical models for MPAMs which itself is an update on the well-known work of Tondu [31]. They have also presented a new mathematical model where the error between the experimental data and the model prediction is less than 7% and the model can handle changes in physical parameters of the actuator with reliable consistency. In this section, for the sake of completeness, we present some of the main mathematical models existing in literature and the improved model presented in [20]. We start with some experimental results obtained with the fabricated MPAM.

Figure 3 shows the end-point deflection versus pressure for a single MPAM. The data is obtained from at least 5 experiments and the mean and the error bars are as shown. We can observe that the tube initially elongates instead of contracting with application of pressure. From detailed observation, it was found that this was due to the initial gap between the braid and the tube in the fabrication process and as a result, the tube expands till it comes in contact with the sheath radially. Once the tube is in contact with the sheath, increase of pressure results in contraction and the maximum contraction was about 20% of the length of the MPAM. Although not shown in the figure, hysteresis was observed. However, the amount of hysteresis was within the error bar and hence we use the mean value between the loading and unloading curves.

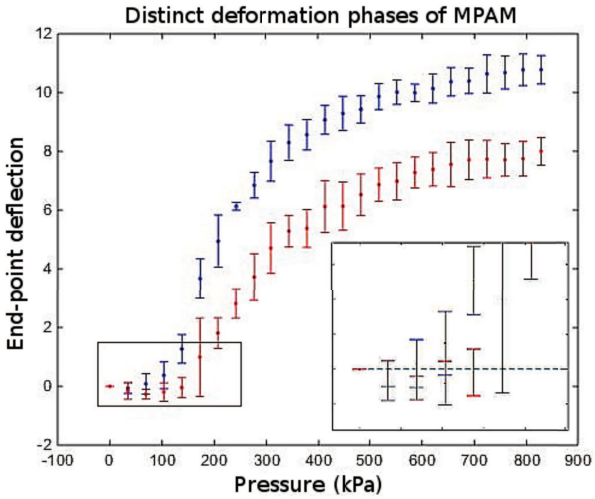

Fig. 3: Deformation phases of MPAM (inset – elongation part zoomed)

One of the earliest attempts in modeling McKibben actuators was made by Schulte [12]. This model was improved upon by considering other physical effects such as friction, material properties, non-uniform shape of cylinder, thermal expansion effect as well as various energy losses [32–34]. When comparing the characteristics of the fabricated MPAM with the deformation profile obtained from models available in the literature, it has been found that most of the models are inaccurate in predicting the deformation of the MPAM. A few models which give good correlation between experimental and theoretical results for one set of initial parameters often generate large errors with changes in one of the parameters (such as initial length or angle of winding) while keeping all the other parameters constant. This is because the models available in the literature are primarily for regular sized PAMs (of diameters up to a few centimeters) and some of the assumptions made in the models may not be applicable to miniaturized PAMs.

3.1 Improved mathematical model for MPAM

Fig. 4 shows the schematic of MPAM with the nomenclature used in modeling the MPAM in this work. The symbols r_o, r_i and l_o denote the outer radius, inner radius and length of inner silicone tube, respectively. The symbols θ_0 and θ denote the angle of winding of MPAM before and after deformation, $\hat{u}_z$ and $\hat{u}_r$ represent axial and radial displacements of braided sleeve while u_z and u_r represent axial and radial displacements of silicone tube. The constant b represents the length of a single braid strand, N denotes the number of windings of braid and P_i is the input pressure. The applied axial load is denoted by F and since the end-effector is assumed to be operating in slow speeds, only static analysis is considered.

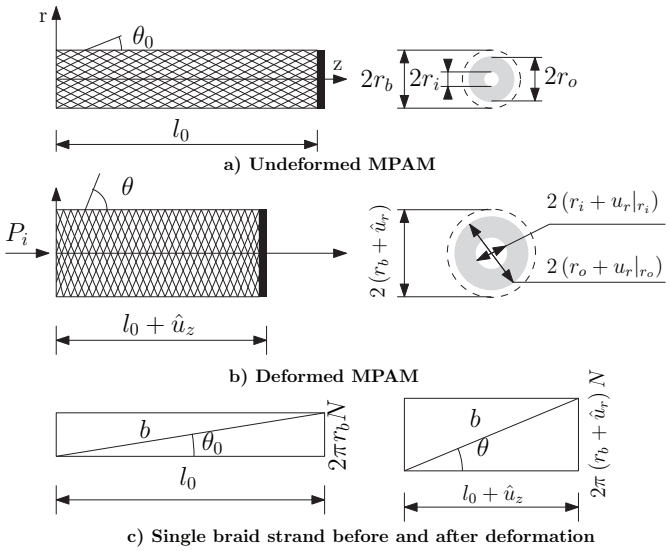

Fig. 4: MPAM nomenclature

As discussed in detail in [20], the model assumes the inner bladder as a linear thick elastic cylinder subjected to inflation and the displacement can be written as

$$u_r = c_1 r + \frac{c_2}{r}, \quad u_z = c_3 z + c_4 \tag{1}$$

where u_r and u_z are the radial and axial displacements, respectively [35]. The constants $c_i, i = 1,2,3,4$ are given by

$$\begin{aligned}
c_1 &= \frac{(\Lambda_1+2\Lambda_2)}{2\Lambda_2(3\Lambda_1+2\Lambda_2)} \times \left[\frac{P_i r_i^2}{r_o^2-r_i^2} + \frac{P_o r_o^2}{r_o^2-r_i^2} - \frac{P_s \Lambda_1}{\Lambda_1+2\Lambda_2}\right] \\
c_2 &= \frac{1}{2\Lambda_2}\left[\frac{r_i^2 r_o^2}{r_o^2-r_i^2}\right](P_i - P_o) \\
c_3 &= \frac{\Lambda_1}{\Lambda_2(3\Lambda_1+2\Lambda_2)} \times \left[-\frac{P_i r_i^2}{r_o^2-r_i^2} + \frac{P_o r_o^2}{r_o^2-r_i^2} + P_s\frac{\Lambda_1+\Lambda_2}{\Lambda_1}\right] \\
c_4 &= 0
\end{aligned} \tag{2}$$

where the quantities P_i, P_o, and P_s are the pressure applied on the inner surface, outer surface and the axial surface of the cylinder, respectively and Λ_1 and Λ_2 are the Lame's constants. Upon applying pressure, the cylinder expands in the axial as well as radial direction. However, for the MPAM, this deformation is restricted by the constraints imposed by the braided sheath. The basic modeling problem is to identify the pressure acting on the outer surface of the tube by the braided sleeve.

As seen in experiments, the tube initially expands due to the gap between the tube and the braid. The critical pressure up to which the tube elongates can be calculated by equating the radius of the braided sheath to the radius of the tube at the contact point:

$$r_o + u_r|_{r_o} = r_o + \delta + \hat{u}_r \tag{3}$$

where δ is the initial gap and $\hat{u}_r$ is the radial displacement of the sheath – which can be expressed in terms of the braid parameters b, N and θ_0. Also, considering that the axial displacement of the tube and the sheath are always same, we can expand the above equation to the form:

$$c_1 r_o + \frac{c_2}{r_o} = \delta + (r_o+\delta)\left\{\frac{1}{\sin\theta_0}\sqrt{1-\cos^2\theta_0\,(1+c_3)^2} - 1\right\} \tag{4}$$

which is a function of the input pressure P_i. Equation (4) can be solved numerically to get the critical pressure P_i^{critical} below which the MPAM expands $\left(P_o = 0, P_s = P_i\frac{r_i^2}{r_o^2-r_i^2} + \frac{F}{\pi r_i^2}\right)$. Above this critical pressure, the tube comes in contact with the sheath and both components displace radially as well as axially by equal amounts, i.e.,

$$c_1 + \frac{c_2}{r_o^2} = \left(\frac{\sin\theta}{\sin\theta_0} - 1\right), \quad c_3 = \left(\frac{\cos\theta}{\cos\theta_0} - 1\right) \tag{5}$$

where the expressions on the right hand side of the equations come from the kinematics of the braid [12].

For the contraction phase, the pressure applied on the outer surface of tube can be calculated by considering the static characteristics of the braided sheath. From the braid statics, we can derive the radial force acting on the outer surface of the tube as [20]

$$F_r = \left(\frac{F_e m \hat{A}_{\text{nyl}} E_{\text{nyl}}}{m\hat{A}_{\text{nyl}}E_{\text{nyl}} + \cos\theta_0 A_{\text{sil}} E_{\text{sil}}}\right)\frac{l_0}{r_o+\delta}\tan\theta\tan\theta_0 \tag{6}$$

Here, $F_e = F + F_{P_i} + F_u$ where F_{P_i} is the force component due to the applied pressure acting on the side walls and F_u are the unaccounted forces such as static friction and axial force component from conical ends etc., which are necessary to maintain the static equilibrium of MPAM. In the above equation E_{sil} and E_{nyl} are the elasticity moduli of silicone and nylon, respectively, A_{sil} and $\hat{A}_{\text{nyl}}$ are the cross-sectional area of silicone tube and a single strand of braid, respectively and m is the number of strands of nylon threads used in the braided sheath.

The quantity F_r is divided by the surface area of contact between the braid and the tube so as to get the outer surface pressure on the cylinder. However, the contact surface area between the sheath and the tube is difficult to measure or to estimate analytically [33, 36] because of the small surface area. We assume that the contact area of braid on surface of tube is same as the contact area between the braid strands at braid cross-over points (refer Fig. 5) and the contact area, in terms of deformed braid angle, is as derived in [36]. It is also observed that at the either ends of the MPAM, the actuator deforms in the form of a conical frustum instead of a perfect cylinder. Based on experimental observations, a full contact is assumed at the surface of the frustums. Considering these

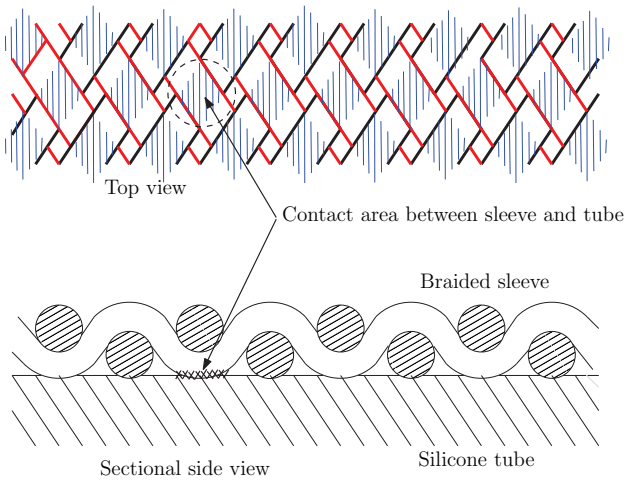

Fig. 5: Contact surface area – assumed to be same as area at the cross-over points

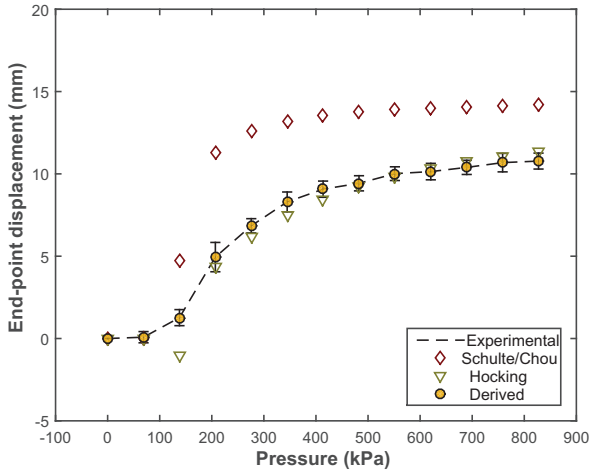

Fig. 6: Comparison for 40 mm MPAM. $\alpha = 36°$, $r_i = 0.25$ mm, $r_o = 0.55$ mm, $r_n = 0.04$ mm, $m = 30$, $\phi = 5$mm, $E = 0.35$ MPa, $\nu = 0.499$.

two assumptions, we can write the contact surface area as

$$S_{\text{contact}} = \frac{\sin^2\theta_{\min}\cos^2\theta_{\min}}{\sin^2\theta\cos^2\theta}\left[2\pi r\left(l_0 - 2\phi\right)\left(1+c_3\right)\right] + 2\pi\left(r_o + \delta + r\right)\phi\left(1+c_3\right) \quad (7)$$

where $\theta_{\min} = \frac{1}{2}\sin^{-1}\left(\frac{r_n m}{\pi r_0}\right)$, r_n denoting the half the diameter of a single strand of braid, and ϕ is the length of the conical frustum which is measured experimentally.

From the contact surface area and the radial force, we get the contact pressure $P_o = F_r/S_{\text{contact}}$. The six equations in (2) and (5) have six unknown quantities viz., c_1, c_2, c_3, c_4, θ and F_u and the unknowns can be solved numerically so as to find the final deformation of the MPAM.

3.2 Comparison of numerical and experimental results

Free contractions of MPAM are calculated numerically using `fsolve` routine in MATLAB and plotted alongside measured values for a pressure range from 0 to 827 kPa (120 psi). Initial model by Schulte [12] as well as the model by Hocking [37] are also plotted for comparison (see [20] for comparison with other models). Fig. 6 shows the plot for deflection of 40 mm long MPAM where it can be seen that theoretical results match experimental values very well. The Young's modulus of the material is obtained as 0.35 MPa by fitting the deformation data on models by Kothera and Hocking. The computation time was approximately 0.04 seconds on an Intel Pentium PC at 2.0 GHz.

For an MPAM of length 60 mm, keeping all the other parameters same, the experimental and computed results are shown in Fig. 7. For both the lengths, the deformation curve is well within the error bounds of measured values. The RMS errors calculated from mean values are 4.6% and 2% of maximum contraction for 40 mm and 60 mm MPAM respectively. The applied force vs axial displacement for a 45 mm MPAM from fully contracted position at 758 kPa (110 psi)

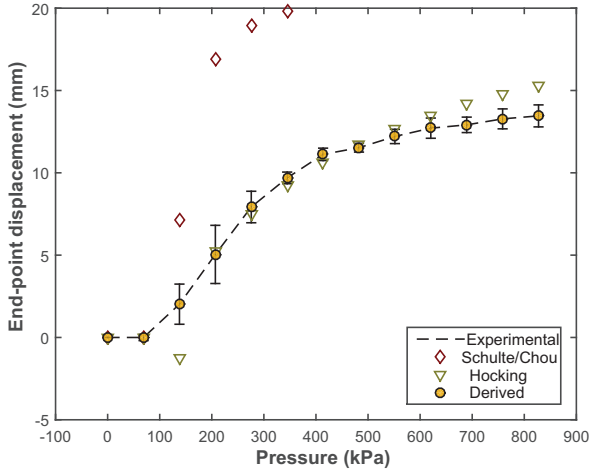

Fig. 7: Comparison for 60 mm MPAM. $\alpha = 36°$, $r_i = 0.25$ mm, $r_o = 0.55$ mm, $r_n = 0.04$ mm, $m = 30$, $\phi = 5$mm, $E = 0.35$ MPa, $\nu = 0.499$.

is plotted in Fig. 8. The stiffness of actuated MPAM predicted by the model (0.94 N/mm) is higher than the actual stiffness (0.63 N/mm) by about 49%. This is because when the applied end load increases, it is experimentally observed that the value of ϕ increases due to the extra stretching of the MPAM. An increase in length of the frustum proportional to the applied end-load ($\hat{\phi} = F/\kappa$ where κ is a constant) shows that the the force characteristics can be better predicted by the model. It may be mentioned that even though Hocking's model shows consistency in change in initial lengths, the model under-predicts the stiffness of the MPAM by more than a factor of 10 since the material properties of the braid is not considered in their formulation.

Through these characterization experiments, we have seen that the developed model is robust, and it can predict the deformation of MPAMs consistently for any value of initial length. After successfully characterizing the MPAMs,

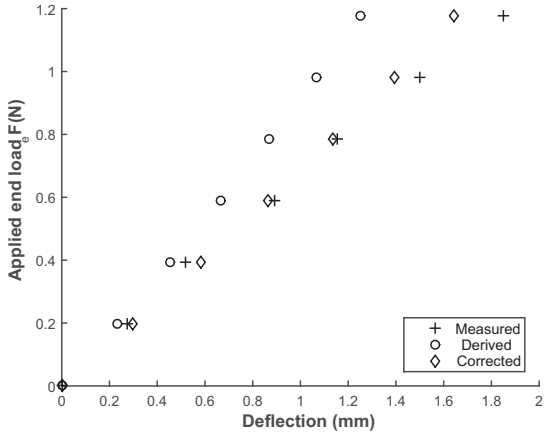

Fig. 8: Axial force vs displacement comparison. $P_i = 758$ kPa, $\alpha = 36°$, $l_o = 45$ mm, $r_i = 0.25$ mm, $r_o = 0.55$ mm, $r_n = 0.04$ mm, $m = 30$, $\phi = 5$mm, $E = 0.35$ MPa, $\nu = 0.499$.

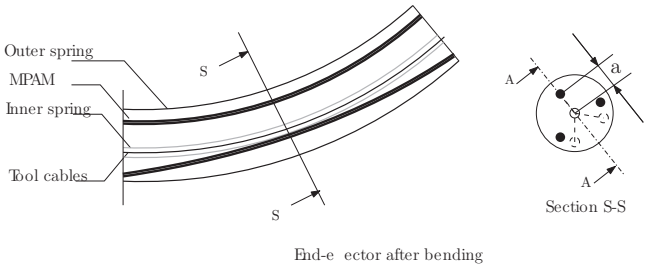

Fig. 9: Tendon driven robot analogy – dotted and filled circles are initial and final position

we employ three of them to actuate the end-effector. The pressure-deformation characteristics shown in this section are utilized in developing the kinematics model of the end-effector.

4 Forward kinematics of end-effector

In the developed end-effector, shown in Fig. 1, there are no guiding disks as in a tendon driven continuum robot. Hence the kinematic analysis procedure used for tendon driven robots (see, for example, [3, 38–40]) cannot be used for the end-effector actuated with MPAMs. Due to the absence of the guiding disks, the MPAMs can drift sideways once the end-effector is deflected as shown in Fig. 9 and, additionally, the radial extension of the tube is not restricted.

To develop a forward kinematic model in the absence of guiding disks, we assume that when the end-effector is deflected, the 3 MPAMs move minimum distance so as to achieve an equilibrium position. Fig. 10 shows the backbone-actuator assembly along an axial section of end-effector (section AA from Fig. 9). The entire length of end-effector is discretized into n segments similar to the pseudo-rigid body models given in [41, 42]. Each segment is a quadrilateral corresponding to a 4-bar linkage, with the following vertices in the unactuated state: 1) the point of contact between one loop of the outer spring and the MPAM 2) the

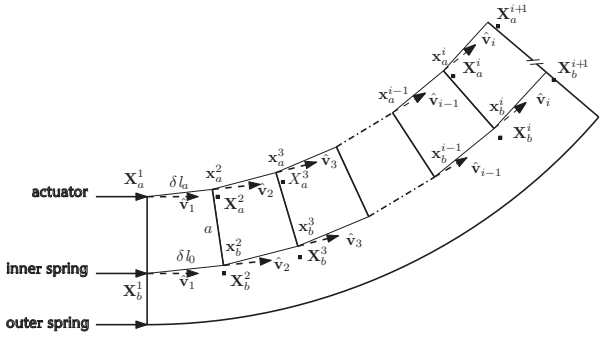

Fig. 10: Backbone-actuator profile

point of contact between the adjacent loop of the outer spring and the MPAM 3) the point in the backbone(axis of the end-effector) closest to vertex (2) and parallel to the ground and 3) the point in the backbone closest to vertex (1) and parallel to the ground. Vertices 1 and 2 form the ends of the first crank of the 4-bar linkage. Vertices 2-3 as well as the vertices 1-4 generate the coupler as well as the fixed links of the linkage respectively. Vertices 3-4 forms the second crank. The lengths of second crank, coupler and the fixed link are always constant while the length of the first coupler changes with respect to the change in length of MPAM during pressurization. An axial force will cause change in length in inner spring. However, since we are only considering transverse loading on the end-effector due to the moment applied by the MPAM, the axial length of the spring (backbone) is assumed to be of constant length throughout the actuation. The length of a backbone in a segment is given as $\delta l_0 = l_0/n$ and the length of actuator in a segment is $\delta l_a = l_a/n$ where l_a is the final length of MPAM after pressurizing. In unactuated state, the segment forms a quadrilateral with coordinates $\mathbf{X}_b^i, \mathbf{X}_b^{i+1}, \mathbf{X}_a^{i+1}, \mathbf{X}_a^i$ as shown in the figure where the subscripts b and a represent backbone and MPAM, respectively and $i = 1$ for segment at the base of end-effector and $i = n$ at the tip. The natural undeformed initial positions $\mathbf{X}_b^{i+1}$ and $\mathbf{X}_a^{i+1}$ are found out as

$$\mathbf{X}_b^{i+1} = \mathbf{X}_b^i + \delta l_0 \hat{\mathbf{v}}_i \text{ and } \mathbf{X}_a^{i+1} = \mathbf{X}_a^i + \delta l_a \hat{\mathbf{v}}_i \tag{8}$$

$$\text{where,} \hat{\mathbf{v}}_i = \frac{\mathbf{X}_b^i - \mathbf{X}_b^{i-1}}{\|\mathbf{X}_b^i - \mathbf{X}_b^{i-1}\|} \tag{9}$$

For the initial segment $i = 1$, the unit vector $\hat{\mathbf{v}}_1$ is perpendicular to the vector $\mathbf{X}_b^1 - \mathbf{X}_a^1$ along the initial axis of end-effector.

After deformation, the quadrilateral changes to $\mathbf{X}_b^i, \mathbf{x}_b^{i+1}, \mathbf{x}_a^{i+1}, \mathbf{X}_a^i$ where vectors in lower case characters represent deformed position (see Fig. 11).

Since the distance between backbone and MPAMs are constrained by the outer spring to a fixed value, the length $\|\mathbf{x}_b^{i+1} - \mathbf{x}_a^{i+1}\| = a$ at all times. The deformed quadrilateral could be positioned in different configurations depending on the angle formed by $\mathbf{x}_a^{i+1} - \mathbf{X}_a^i$ and $\mathbf{X}_b^i - \mathbf{X}_a^i$. Here, the natural configuration is assumed to be the one which minimizes the displacement of tip $\mathbf{x}_a^{i+1}$ [43]. To find the deformed con-

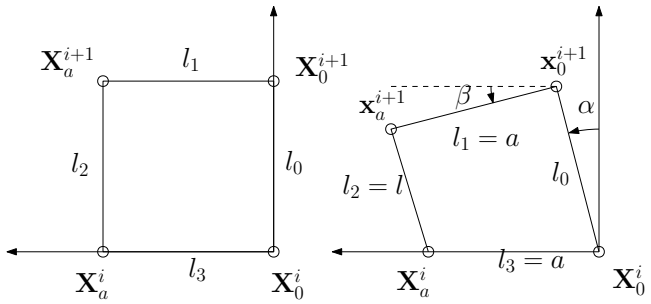

Fig. 11: Nomenclature of a single segment

figuration, we formulate an optimization problem

$$\begin{aligned} &\min_{\mathbf{x}_b^{i+1},\mathbf{x}_a^{i+1}} \|\mathbf{X}_a^{i+1} - \mathbf{x}_a^{i+1}\| \\ &\text{Subject to :} \quad \|\mathbf{x}_b^{i+1} - \mathbf{X}_b^i\| = \delta l_0, \\ &\|\mathbf{x}_a^{i+1} - \mathbf{X}_a^i\| = \delta l_a, \quad \|\mathbf{x}_b^{i+1} - \mathbf{x}_a^{i+1}\| = a \end{aligned} \tag{10}$$

The solution to the above optimization problem gives the co-ordinates of tips $\mathbf{x}_b^{i+1}$ and $\mathbf{x}_a^{i+1}$. The iterative method starts from the base segment and proceeds towards the tip of the end-effector to determine the final pose of the end-effector backbone and the actuated MPAM. One can also see that that the above minimization problem also translates to finding the co-ordinates $\mathbf{x}_0^{i+1}$ and $\mathbf{x}_a^{i+1}$ when the tip $\mathbf{x}_a^{i+1}$ simply retracts inwards, as the MPAM compresses in its axial direction. From this reasoning, the above equation can be simplified by considering the corresponding geometric relations of the four-bar linkage

$$\delta l_0 \sin\alpha + a\cos\beta = a, \quad \delta l_0 \cos\alpha - a\sin\beta = \delta l_a \tag{11}$$

where α is the angle made by the first crank (corresponding to the backbone) with the vertical axis, and β is the coupler angle. The above equations are much faster to solve compared to the optimization routine, and we can find the value of α. Once α is found out, we can get the co-ordinate of the tip as

$$\mathbf{x}_0^{i+1} = (\delta l_0 \sin\alpha,\ \delta l_0 \cos\alpha)^T \tag{12}$$

and the co-ordinates of the tip of the end-effector in the plane of bending of the end-effector is given as:

$$\mathbf{x}_0^n = \begin{bmatrix} \delta l_0 (\sin\alpha + \sin 2\alpha + \cdots + \sin(n-1)\alpha) \\ \delta l_0 (\cos\alpha + \cos 2\alpha + \cdots + \cos(n-1)\alpha) \end{bmatrix} \tag{13}$$

The iterative scheme for solution to the forward kinematics of end-effector, considering the MPAM statics, can be summarized as

1. Obtain the deformation of a single MPAM, for zero applied axial force, from the mathematical model discussed in section 3.1. From the deformation, compute δl_a.
2. Compute the coordiantes of the tips either from the optimization problem in (10) or using equation (13) and obtain the pose of end-effector.
3. The displacement of tip δ_e from the original position is calculated from the obtained pose of the end-effector.
4. The moment that need to be applied at the tip of end-effector to produce the same deflection is calculated using the cantilever equation $\delta_e = ML^2/3EI$, where EI is the flexural rigidity of the end effector. From the moment, using $M = a \times F$, compute the axial force F that should be produced by the MPAM in order to get the same deflection.
5. Using the computed F, the deformation of single MPAM is re-calculated and the same procedure is repeated till the change in final deflection of end-effector is within a specified tolerance.

From several experiments of actuating three MPAMs individually, it is found out that the MPAMs are at 307.5°, 219° and 75° angles from the positive $\hat{\mathbf{i}}$ axis shown in Fig. 14. These are named *R*, *G* and *B* respectively for identification. By applying a 0.1 N transverse load at the tip of the end-effector, a deflection of approximately 15 mm is obtained. The flexural rigidity is then calculated using the standard beam equation.

In case two MPAMs are actuated together, the resultant moment due to these actuations can be written as

$$\mathbf{M} = \mathbf{a}_i \times \mathbf{F}_i + \mathbf{a}_j \times \mathbf{F}_j = \mathbf{a}_r \times \mathbf{F}_{\text{res}} \tag{14}$$

where $\mathbf{a}_{i,j}$ are the position vectors of the tip of i^{th} and j^{th} MPAM and $\mathbf{F}_{i,j}$ are the applied forces on end-effector by the MPAMs, $\mathbf{a}_r$ is the position vector of a hypothetical actuator whose resultant force $F_{\text{res}} = F_1 + F_2$ will provide the same moment as due to the other two MPAMs actuated together (see Fig. 12(a)). From mechanics, the direction of the hypothetical actuator is given by

$$l_r = \frac{(l_1F_1 + l_2F_2)}{F_1 + F_2}, \quad m_r = \frac{(m_1F_1 + m_2F_2)}{F_1 + F_2} \tag{15}$$

where $l_i, m_i,\ i = 1,2$ determine the directions of $\mathbf{F}_1$ and $\mathbf{F}_2$ and l_r, m_r also determine the plane of bending of the end-effector.

If two MPAMs are pressurized simultaneously, the axial force generated at the tip will be large enough to compress the inner spring. Hence, MPAMs are pressurized one at a time. From Fig. 12(b), the tip deflection from initial position ξ_0 due to individual actuation of two MPAMs (given by curves ξ_1 and ξ_2) are along the direction of force vectors represented by $\mathbf{d}_1$ and $\mathbf{d}_2$, respectively. When these MPAMs are pressurized successively, with $\mathbf{d}_1$ followed by $\mathbf{d}_2$, the vector $\mathbf{d}_2$ is rotated by β_1 angle. The resultant deflection will be in the direction of vector sum of $\mathbf{d}_1$ and $\mathbf{d}_2'$ where $\mathbf{d}_2' = \hat{\mathbf{R}}_{(\hat{\mathbf{q}}_1,\beta_1)}\mathbf{d}_2$ is the rotated vector (see Fig. 12(c)).

The following steps summarize the method in finding the final pose of end-effector when two MPAMs (say R and G) are actuated:

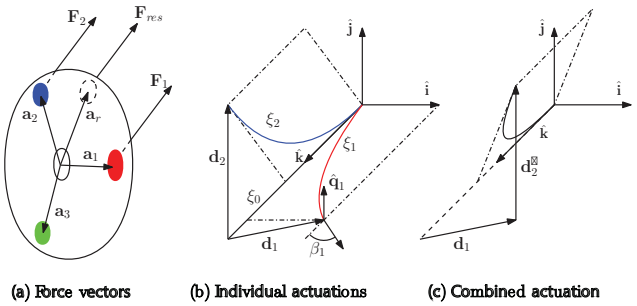

Fig. 12: Displacement vector addition

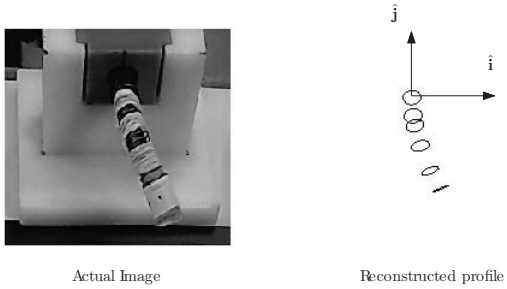

Fig. 13: Profile reconstruction using image analysis

1. Pose of end-effector ξ_1 when MPAM-R is pressurized individually is found out using the above formulation; tip deflection vector $\mathbf{d}_1$ is calculated. Likewise ξ_2 is found out when MPAM-G is pressurized individually and corresponding $\mathbf{d}_2$ is calculated.
2. Angle of end-point vector of MPAM-R is calculated using the equation:

$$\beta_1 = \cos^{-1}\left(\frac{\mathbf{x}_b^n - \mathbf{x}_b^{n-1}}{\|\mathbf{x}_b^n - \mathbf{x}_b^{n-1}\|}\cdot\hat{\mathbf{k}}\right) \tag{16}$$

3. Axis vector $\hat{\mathbf{q}}_1$ is found out using the equation:

$$\hat{\mathbf{q}}_1 = \frac{\mathbf{x}^n - \mathbf{x}^{n-1}}{\|\mathbf{x}^n - \mathbf{x}^{n-1}\|} \times \frac{\mathbf{x}^{n-2} - \mathbf{x}^{n-1}}{\|\mathbf{x}^{n-2} - \mathbf{x}^{n-1}\|} \tag{17}$$

4. Rotation matrix $\hat{\mathbf{R}}_{(\hat{\mathbf{q}}_1,\beta_1)}$ is populated using axis-angle method [44] and tip displacement of second MPAM (MPAM-G), $\mathbf{d}_2$ is rotated to get $\mathbf{d}_2'$.
5. Direction cosines of $\mathbf{a}_r$ are calculated using (15). The plane containing the vector $\mathbf{a}_r$ as well as the $\hat{\mathbf{k}}$ axis can be defined by its normal vector $(m_r)\hat{\mathbf{i}} + (-l_r)\hat{\mathbf{j}}$.
6. A straight line is drawn from the vector $l_0\hat{\mathbf{k}} + \mathbf{d}_1$ in the direction of $\mathbf{d}_2'$. The intersection of this line with the plane defined in step 4) gives the final tip position.
7. The iteration is repeated with $n \to n-1$ for the entire length of end-effector to obtain the final pose.

In summary, from the static model of MPAM derived in section 3.1, we obtain the deformed length corresponding to an applied pressure and axial load. From the forward kinematic equations derived in this section, we get the pose of end-effector corresponding to given displacement of MPAMs/tendons. Combining both the models, we obtain the pose of end-effector corresponding to pressure applied at MPAMs.

4.1 Experimental validation

In order to validate the developed model, the prototype end-effector is subjected to different values of pressure and the pose of end-effector after deflection is compared with the values obtained from computations. Two cameras are used to

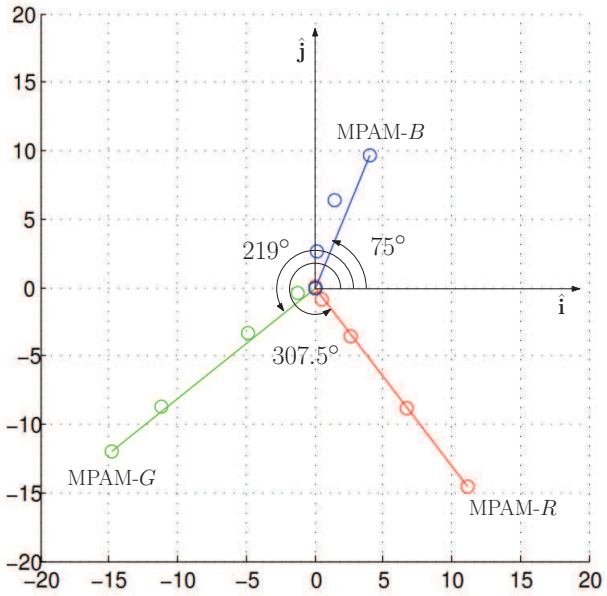

Fig. 14: MPAM positioned in the three directions

capture images from different angles and the 3D co-ordinates of the central (backbone) curve of end-effector is obtained using multiple view image reconstruction techniques [45]. A thin flexible film of white colour is applied on the end effector surface to facilitate control point identification. A high contrast marking is made at the tip so that the marker is easily identified in the images. To find the co-ordinates of the tip, respective pixels in the two images corresponding to the marker position is manually selected. The possible error in this method is in incorrectly identifying the marker pixels and this is not more than 4 pixels size for both the images. For the scale and measurement set up used, the maximum error in reconstruction is approximately 2 mm at the tip.

Fig. 13 shows the deformation of end-effector as well as the re-constructed profile when one MPAM is pressurized. In the figure, the reconstructed profile is shown up to 45 mm from the base of the MPAM while due to the holder the end-effector tip extends up to 55 mm.

As a numerical illustration, a pressure of 689.4 kPa (100 psi) is applied to the MPAM labeled *R* (refer Fig. 13). For zero applied axial force, we get $\Delta = 7.6$ mm contraction as per the mathematical model. The final length of MPAM will

Table 1: R at $P_i = 689.4$ kPa

F (N)	Δ (mm)	δ_e (mm)	F^* (N)
0	7.6	22.8	1.69
1.69	6.9	20.4	1.51
1.51	6.9	20.4	1.51

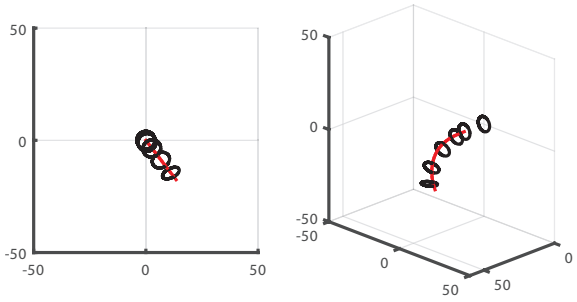

Fig. 15: MPAM R actuated at 689.4 kPa

be $l_a = l_o - \Delta = 37.4$ mm. This value is used to predict the pose of end-effector using the kinematic model where 15 segments are used for computation – the length of one segment is equal to the pitch of the outer spring. The final pose of end-effector gives a tip deflection of $\delta_e = 22.8$ mm. The force F which MPAM has to apply on end-effector so as to obtain this value of deflection is calculated to be $F^* = 1.69$ N. Now, the deformation of MPAM is re-calculated with $F = F^* = 1.69$ N force where the deflection is 6.9 mm for 45 mm MPAM. The procedure is repeated as shown in Table 1 and one can see that the iterative approach converges with the deformation of MPAM to achieve equilibrium as 6.9 mm. The pose of end-effector obtained with final length of MPAM as 38.1 mm $(45 - 6.9)$ is shown in Fig. 15 alongside the actual deflection of end-effector. The measured pose of the end-effector matches with the computation with a maximum error of 1 mm at the tip. The time required to solve the forward kinematics is about 0.6 seconds on an Intel Pentium PC at 2.0 GHz.

Fig. 16 shows the comparison between the computed and measured pose for MPAM-G actuated at 551.6 kPa (80 psi). The maximum error in tip deflection in this case is also found to be about 1 mm. Fig. 17 shows the final deformation of end-effector when two MPAMs are actuated by the same pressure of 689.4 kPa (100 psi). The experimental results, in this case too, agree with the iterative approach with approximately 1 mm error at the tip.

When the two MPAMs are applied different pressures, the same iterative approach can be used. As an example, the deformation and axial force for a 413 kPa (60 psi) pressure input are 15.8 mm and 1.17 N, respectively. The direction cosines of $\mathbf{a}_r$ calculated using $F_1 = 1.51$ N (corresponding to 689 kPa pressure) and $F_2 = 1.17$ N (corresponding to 413 kPa pressure) are $l_r = -0.17$ and $m_r = -0.7$, respectively–

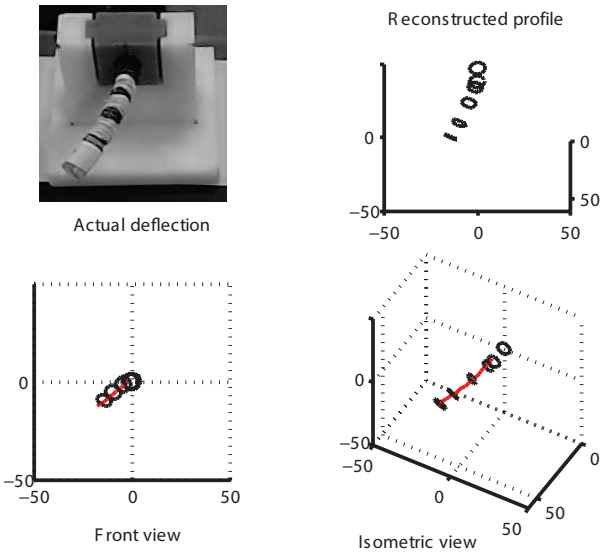

Fig. 16: MPAM G actuated at 551.6 kPa

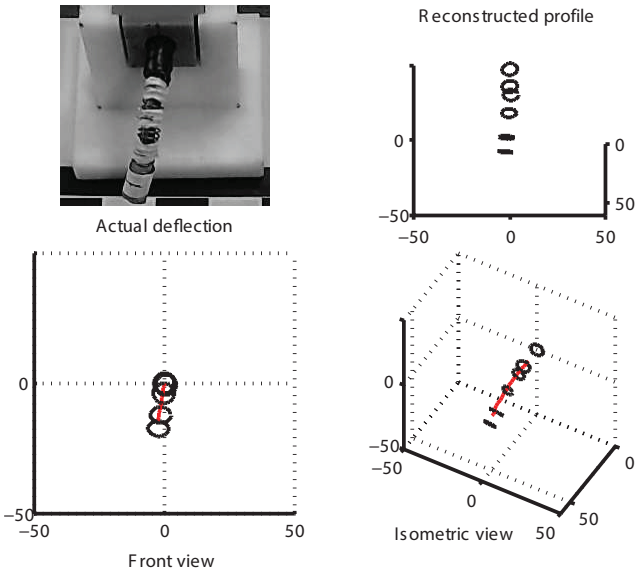

Fig. 17: MPAMs R, G actuated at 689.4 kPa

i.e., the plane forms an angle 13.3° with the $\hat{j}$ axis. When 413 kPa is applied on MPAM-R and 689 kPa on MPAM-G, the reconstructed profile and the computed results are shown in Fig. 18.

5 Inverse kinematics of end-effector

The inverse kinematics problem of the end-effector corresponds to finding the pressure required in different MPAMs so as to position the tip at a given point in the workspace of the end-effector. The endoscopist can only specify a point in the workspace as a point on the images from the endoscopic camera feed. Hence, we use a 2-D projection of the end-effector workspace to specify the point to be achieved by the tip.

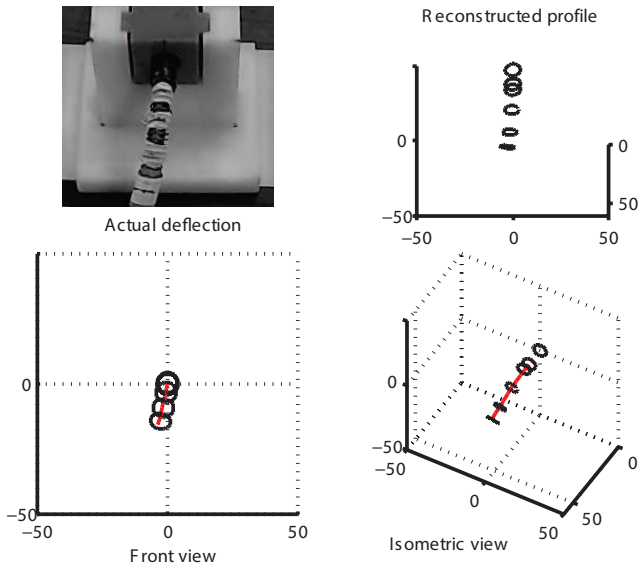

Fig. 18: MPAM G at 689.4 kPa and R at 413 kPa

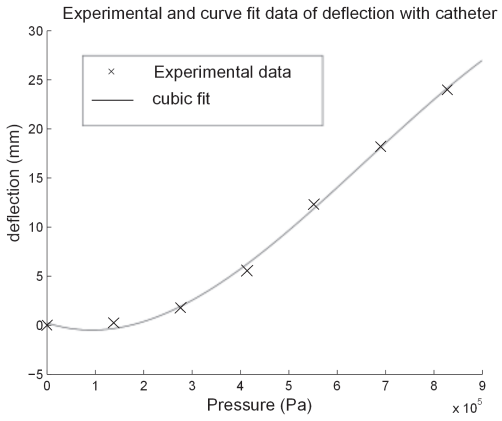

Fig. 20: Increase in the deflection of tip of catheter from the initial position with applied pressure

5.1 Inverse kinematics model

In Fig. 19, the front view of an end-effector is shown, with a commercially available forceps catheter inserted through the inner spring. Fig. 20 shows the pressure vs deflection profile for the catheter tip and a cubic curve is fitted to the data to visualize the deflection profile. The end-effector generates a maximum deflection of about 25 mm from the axis at 827 kPa pressure.

For inverse kinematics analysis, we first project the workspace to the front view of the end-effector – front view is chosen for better visualization of results, any other projection can also be used – which takes the shape of a hexagon as shown in Fig. 21. By applying maximum pressure

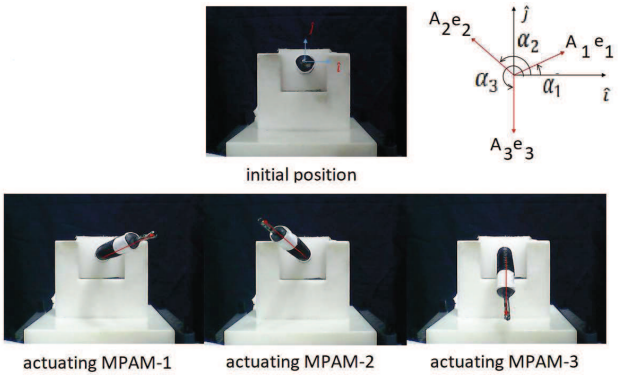

Fig. 19: Front view of end-effector

in three MPAMs individually, we get the end-effector tip-deflections in three different directions as shown in Fig. 19. If we consider position of the un-actuated end-effector tip as the origin, we get three displacement vectors in the directions $\mathbf{e}_1, \mathbf{e}_2$, and $\mathbf{e}_3$ corresponding to the MPAMs R, G

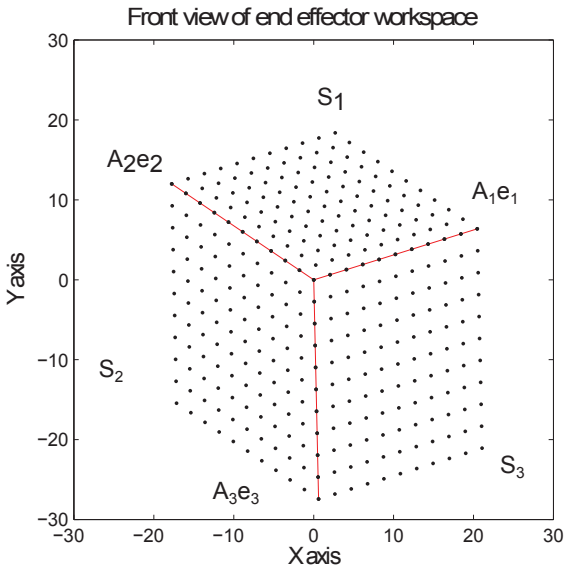

Fig. 21: Workspace of end-effector

and B. Then the entire workspace is spanned by the combination of vectors $A_1\mathbf{e}_1$, $A_2\mathbf{e}_2$, and $A_3\mathbf{e}_3$ which correspond to the maximum displacement in the respective directions. The vectors divide the projected workspace into three sectors $S_i, i = 1,2,3$ which is spanned by the vectors $A_i\mathbf{e}_i$ and $A_j\mathbf{e}_j$, where $i = 1,2,3$ and $j = 2,3,1$ in that order.

In order to achieve a particular point in the projected workspace of the end-effector, say $\mathbf{v} = (v_x, v_y)^T$, the MPAMs i and j should be pressurized so as to get the deflections a_i and a_j as shown in Fig. 22. Given the co-ordinates of the vector in Cartesian space, it can be resolved in to the directions $\mathbf{e}_i$ and $\mathbf{e}_j$ as

$$v_x\hat{\mathbf{i}} + v_y\hat{\mathbf{j}} = \left[\frac{v_x \sin\alpha_j - v_y \cos\alpha_j}{\sin(\alpha_j - \alpha_i)}\right]\mathbf{e}_i + \left[\frac{-v_x \sin\alpha_i + v_y \cos\alpha_i}{\sin(\alpha_j - \alpha_i)}\right]\mathbf{e}_j \quad (18)$$

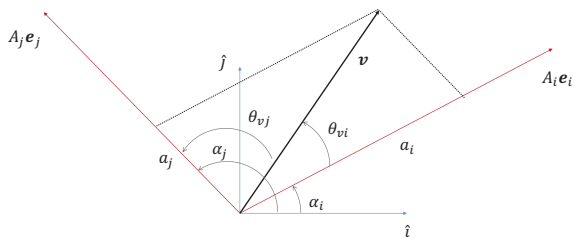

Fig. 22: Vector in workspace

where the angles α_i and α_j are measured from the positive $\hat{\imath}$ axis.

Once the required deflections a_i and a_j are found, the pressure required to achieve these tip deflections can be obtained from the forward kinematics model. We know the number of segments 'n' from the design specifications. The deflection a_i in the projected plane is the second component of the vector $\mathbf{x}_0^n$ given in equation (13). However, the information about the first component is usually lost in the projection and we use a look-up table, containing the pressure-deflection profile obtained from the forward kinematics model explained in section 4, for easy implementation.

5.2 Experimental validation and real-time implementation

For a chosen point in the projected end-effector workspace, Fig. 23 and Fig. 24 show the expected and actual position of the end-effector tip. MPAM-R is applied a pressure of 689 kPa and MPAM-G is applied 827 kPa (maximum pressure). The predicted deflection and the actual deflection shows a maximum error of 9° at the farthest reach of the end-effector. It may be noted that the aforementioned inverse kinematics model is an open-loop control. A model-based control strategy, using the forward kinematics model could reduce the error significantly.

In order to prove the viability of application in a real-time setting, the end-effector is coupled with a thumb-stick for actuation so that moving the thumb-stick may generate equivalent motion of the tip of the end-effector. In order to achieve this, the projected workspace of the end-effector is superimposed on the workspace of the thumb-stick–which is a square surface. From the thumb-stick, we get analog signals ranging from -512 to +512 in left-right and top-bottom directions. One unit of thumb-stick motion equals to $\dfrac{\max\{A_i, \|A_i\mathbf{e}_i + A_j\mathbf{e}_j\|\}}{512}$ mm, with $i, j = 1,2,3$. Using this conversion scale, a particular position of the thumb-stick chosen by the user will give the corresponding (v_x, v_y) co-ordinate. A sector in the workspace, S_i may be calculated using the condition $\theta_{vi} + \theta_{vj} = \alpha_j - \alpha_i$; θ_{vi} and θ_{vj} being the angle made by vector $\mathbf{v}$ with the unit vectors $\mathbf{e}_i$ and $\mathbf{e}_j$, respectively as shown in Fig. 22. Once the sector is determined, the corresponding deflections and thus, the required pressure values are found out as described in section 5.1.

Since the projected workspace of the end-effector is a

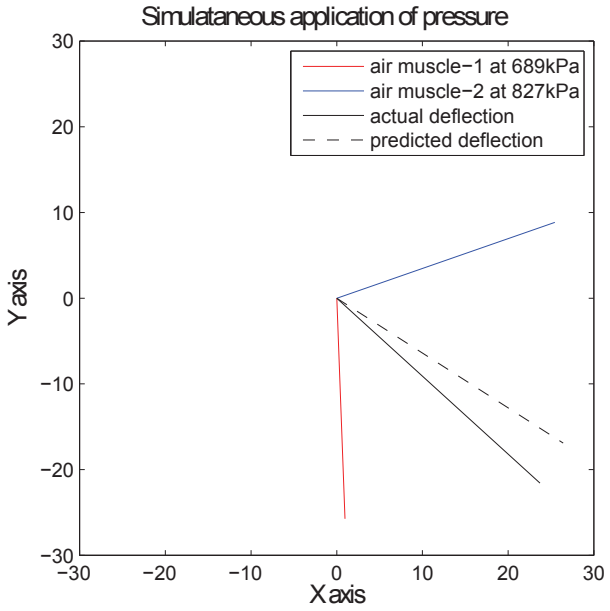

Fig. 23: Experimental vs Theoretical comparison of deflection in random direction

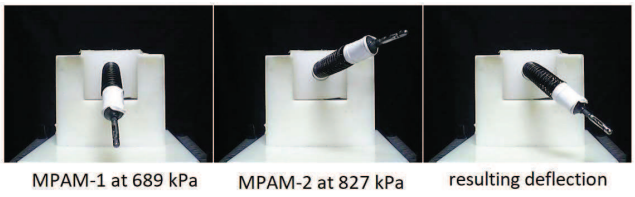

Fig. 24: Deflection in resultant direction

hexagon and the thumb-stick workspace is a square, some co-ordinates chosen in the thumbstick may lie outside the workspace of the end-effector. Those outliers are approximated to the nearest point in the workspace, along the line connecting the point and the origin, as shown in Fig. 25.

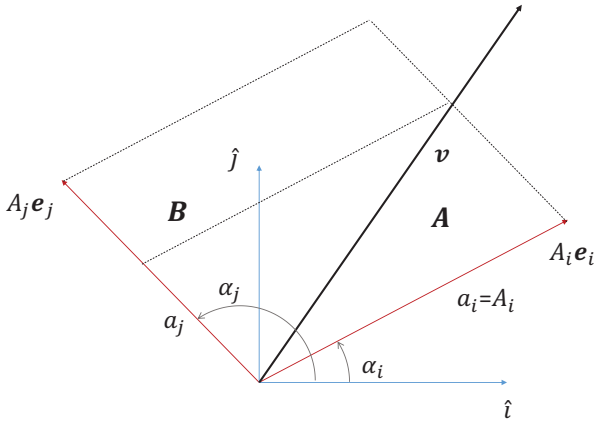

Fig. 25: Vector outside workspace

5.3 Results and discussion

A number of experiments were conducted on the end-effector and it is found to be possible to position the tip of a catheter at a particular chosen point in the projected workspace of the end-effector. Representative points are shown in Fig. 26, where the tip of the end-effector is made to trace a line. The pressure applied on different MPAMs R, G and B are also shown in the figure. Red crosses represent the points when single muscle is actuated and the blue crosses show the points where two MPAMs are used for actuation. Fig. 27 shows the points tracked by the end-effector when the thumb-stick is moved in a circle. The corresponding pressure values are also shown in the figure.

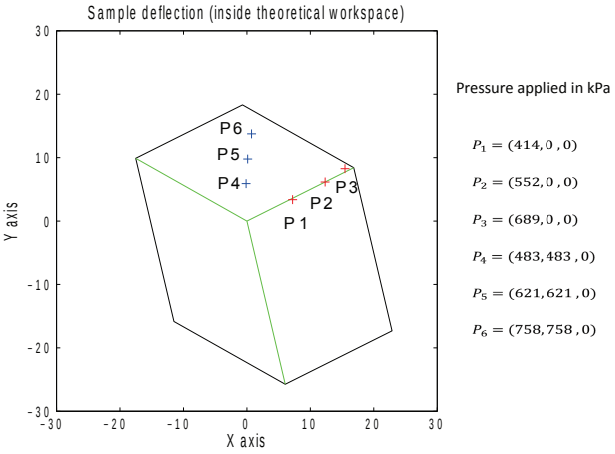

Fig. 26: End-effector tip tracing line in workspace. Shown in brackets are the pressure applied on MPAM-R,G and B in that order.

From experiments, the maximum lateral force generated at the tip of the end-effector is found to be 0.2 N. While it is shown that the force is enough to manipulate a catheter, it is not sufficient to generate the puncture forces required to perforate the tissues [46]. Unlike rigid mechanisms, the developed end-effector uses pressure control instead of position control. Hence, even if the endoscopist accidentally specifies a point under the tissue walls, the inherent compliance of the device ensures that tissue damages will not occur (refer Fig. 28). From our preliminary ex-vivo experiments conducted on pig tissue [47], we have observed that the prototype end-effector does not cause perforation even at high values of applied pressure of 827 kPa[1].

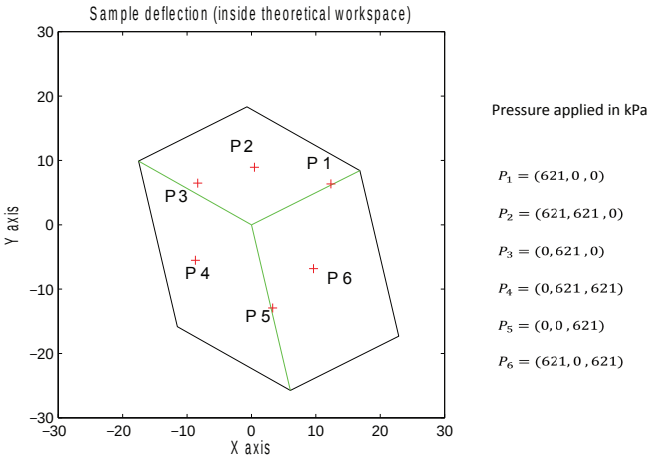

Fig. 27: End-effector tip tracing circle in workspace. Shown in in brackets are the pressure applied on MPAM-R,G and B in that order.

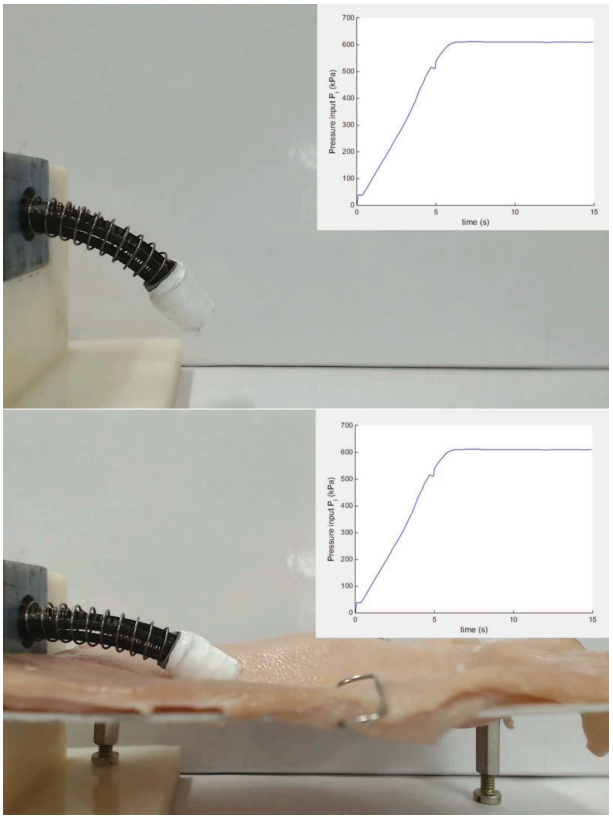

Fig. 28: End-effector does not perforate the tissue at highest actuation pressure

6 Conclusions

This paper deals with the modeling, analysis and experimental validation of a novel independently actuated flexible endoscopic end-effector. The end-effector presented in this work is actuated by three miniaturized pneumatic artificial muscles (MPAM) and it does not have guiding discs used in other cable driven system. The kinematics of the actuated end-effector, taking into account the absence of guiding discs, is formulated as a constrained optimization problem. Using a derived mathematical pressure-deformation relationship for an MPAM, first the change in length in one or more

[1]Experiments were conducted on tissue samples taken from different sections of a porcine GI tract such as stomach, intestine and upper GI tract.

of the pressurized MPAMs is obtained and then the position and orientation of the end-effector is obtained using an iterative scheme. Experiments performed on the developed prototype show that the end-effector tip can be positioned in an approximate hemispherical section of 45 mm radius. Using 3D profile reconstruction of the images obtained during experimentation, it is shown that the maximum position error at the tip of the end-effector between numerical predictions and the experiments is 2 mm. The developed forward kinematics formulation thus shows promise for use in model based control strategies.

In this work, we also presented an inverse kinematics algorithm where for a chosen point on the projected workspace of the end-effector, the pressure required to reach that point can be computed. The results from the computational model and the experimental results deviate by approximately 9° at the farthest reach of the end-effector. The end-effector is then integrated with a thumb-stick to demonstrate the possibility of real-time actuation. Ex-vivo experiments conducted on a pig tissue shows that the end-effector does not cause any perforation of the tissue during actuation.

At present, we are working towards reducing the overall diameter of the end-effector. Additionally, we are making attempts to reduce the error by developing model-based control strategies. Currently, the computation time for the forward kinematics is of the order of 0.6 seconds on a desktop PC and this is due to the iterative solution of the constrained optimization problem. Attempts are being made to reduce this time for efficient real-time control. While the developed proof of concept shows that MPAM based end-effector has definite advantages in endoscopic catheter actuation, significantly more work is required before the same can be employed in a clinical setting and we are working towards achieving this goal.

Acknowledgement

This work was partly funded by a grant from the Robert Bosch Centre for Cyber Physical System, Indian Institute of Science, Bangalore.

References

[1] Yeung, B. P. M., and Gourlay, T., 2012. "A technical review of flexible endoscopic multitasking platforms". *International Journal of Surgery,* **10**(7), pp. 345–354.

[2] Zorn, L., Nageotte, F., Zanne, P., Legner, A., Dallemagne, B., Marescaux, J., and de Mathelin, M., 2018. "A novel telemanipulated robotic assistant for surgical endoscopy: Pre-clinical application to ESD". *IEEE Transactions on Biomedical Engineering,* **65**(4), pp. 797–808.

[3] Gravagne, I. A., and Walker, I. D., 2000. "On the kinematics of remotely-actuated continuum robots". In IEEE Conference on Robotics and Automation, April 24-28, 2000, San Francisco, USA, Vol. 3, pp. 2544–2550.

[4] Xu, K., Goldman, R. E., Ding, J., Allen, P. K., Fowler, D. L., and Simaan, N., 2009. "System design of an insertable robotic effector platform for single port access (SPA) surgery". In IEEE/RSJ International Conference on Intelligent Robots and Systems, October 11-15, 2009, St Louis, USA pp. 5546–5552.

[5] Szewczyk, J., De Sars, V., Bidaud, P., and Dumont, G., 2001. "An active tubular polyarticulated micro-system for flexible endoscope". *Experimental Robotics VII*, pp. 179–188.

[6] Kumbhari, V., and Khashab, M. A., 2014. "Perforation due to ERCP". *Techniques in Gastrointestinal Endoscopy,* **16**(4), pp. 187–194.

[7] De Greef, A., Lambert, P., and Delchambre, A., 2009. "Towards flexible medical instruments: Review of flexible fluidic actuators". *Precision Engineering,* **33**(4), pp. 311–321.

[8] Marchese, A. D., Komorowski, K., Onal, C. D., and Rus, D., 2014. "Design and control of a soft and continuously deformable 2D robotic manipulation system". In IEEE International Conference on Robotics and Automation, May 31 - June 5, 2014, Hongkong, China, pp. 2189–2196.

[9] Rus, D., and Tolley, M. T., 2015. "Design, fabrication and control of soft robots". *Nature,* **521**(7553), p. 467.

[10] Stapfer, M., Selby, R. R., Stain, S. C., Katkhouda, N., Parekh, D., Jabbour, N., and Garry, D., 2000. "Management of duodenal perforation after endoscopic retrograde cholangiopancreatography and sphincterotomy". *Annals of Surgery,* **232**(2), p. 191.

[11] Gaylord, R. H., 1958. Fluid actuated motor system and stroking device, 22. US Patent 2,844,126.

[12] Schulte, H., 1961. "The application of external power in prosthetics and orthotics". *The Characteristics of the McKibben Artificial Muscle, National Research Council,* **874**.

[13] De Volder, M., Moers, A., and Reynaerts, D., 2011. "Fabrication and control of miniature mckibben actuators". *Sensors and Actuators A: Physical,* **166**(1), pp. 111–116.

[14] Chakravarthy, S., Aditya, K., and Ghosal, A., 2014. "Experimental characterization and control of miniaturized pneumatic artificial muscle". *ASME Trans., Journal of Medical Devices,* **8**(4), p. 041011.

[15] Kurumaya, S., Nabae, H., Endo, G., and Suzumori, K., 2017. "Design of thin mckibben muscle and multifilament structure". *Sensors and Actuators A: Physical,* **261**, pp. 66–74.

[16] Trivedi, D., Rahn, C. D., Kier, W. M., and Walker, I. D., 2008. "Soft robotics: Biological inspiration, state of the art, and future research". *Applied Bionics and Biomechanics,* **5**(3), pp. 99–117.

[17] Vocke III, R. D., Kothera, C. S., Chaudhuri, A., Woods, B. K., and Wereley, N. M., 2012. "Design and testing of a high-specific work actuator using miniature pneumatic artificial muscles". *Journal of Intelligent Material Systems and Structures,* **23**(3), pp. 365–378.

[18] Sardellitti, I., Park, J., Shin, D., and Khatib, O., 2007. "Air muscle controller design in the distributed macro-mini (DM 2) actuation approach". In IEEE/RSJ International Conference on Intelligent Robots and Systems, October 29 - November 2, 2007, San Diego, USA,

pp. 1822–1827.

[19] Andrikopoulos, G., Nikolakopoulos, G., and Manesis, S., 2011. "A survey on applications of pneumatic artificial muscles". In 19th Mediterranean Conference on Control & Automation, June 20-23, 2011, Corfu, Greece, pp. 1439–1446.

[20] Ashwin, K. P., and Ghosal, A., 2018. "A survey on static modeling of miniaturized pneumatic artificial muscles with new model and experimental results". *ASME Trans., Applied Mechanics Reviews,* **70**(4), p. 040802.

[21] Banerjee, H., Pusalkar, N., and Ren, H., 2018. "Single-motor controlled tendon-driven peristaltic soft origami robot". *ASME Trans., Journal of Mechanisms and Robotics,* **10**(6), p. 064501.

[22] Büchler, D., Ott, H., and Peters, J., 2016. "A lightweight robotic arm with pneumatic muscles for robot learning". In IEEE International Conference on Robotics and Automation, May 16-21, 2016, Stockholm, Sweden, pp. 4086–4092.

[23] Li, H., Kawashima, K., Tadano, K., Ganguly, S., and Nakano, S., 2013. "Achieving haptic perception in forceps manipulator using pneumatic artificial muscle". *IEEE/ASME Transactions on Mechatronics,* **18**(1), pp. 74–85.

[24] Kang, R., Branson, D. T., Zheng, T., Guglielmino, E., and Caldwell, D. G., 2013. "Design, modeling and control of a pneumatically actuated manipulator inspired by biological continuum structures". *Bioinspiration & Biomimetics,* **8**(3), p. 036008.

[25] Jamwal, P. K., Xie, S. Q., Hussain, S., and Parsons, J. G., 2014. "An adaptive wearable parallel robot for the treatment of ankle injuries". *IEEE/ASME Transactions on Mechatronics,* **19**(1), pp. 64–75.

[26] Kang, R., Guo, Y., Chen, L., Branson III, D. T., and Dai, J. S., 2017. "Design of a pneumatic muscle based continuum robot with embedded tendons". *IEEE/ASME Transactions on Mechatronics,* **22**(2), pp. 751–761.

[27] Connolly, F., Walsh, C. J., and Bertoldi, K., 2017. "Automatic design of fiber-reinforced soft actuators for trajectory matching". *Proceedings of the National Academy of Sciences,* **114**(1), pp. 51–56.

[28] Liu, Y., Zang, X., Liu, X., and Wang, L., 2015. "Design of a biped robot actuated by pneumatic artificial muscles". *Bio-medical Materials and Engineering,* **26**(s1), pp. S757–S766.

[29] Ashwin, K., Jose, D. P., and Ghosal, A., 2015. "Modeling and analysis of a flexible end-effector for actuating endoscopic catheters". In Proceedings of the 14th IFToMM World Congress, October 25-30, 2015, Taipei, Taiwan, pp. 113–120.

[30] MATLAB, 2011. "7.12. 0.635 (r2011a) The MathWorks Inc.". *Natick, Massachusetts, United States*.

[31] Tondu, B., 2012. "Modelling of the mckibben artificial muscle: A review". *Journal of Intelligent Material Systems and Structures,* **23**(3), pp. 225–253.

[32] Tondu, B., and Lopez, P., 2000. "Modeling and control of mckibben artificial muscle robot actuators". *IEEE Control Systems,* **20**(2), pp. 15–38.

[33] Chen, D., and Ushijima, K., 2014. "Prediction of the mechanical performance of Mckibben artificial muscle actuator". *International Journal of Mechanical Sciences,* **78**, pp. 183–192.

[34] Andrikopoulos, G., Nikolakopoulos, G., and Manesis, S., 2016. "Novel considerations on static force modeling of pneumatic muscle actuators". *IEEE/ASME Transactions on Mechatronics,* **21**(6), pp. 2647–2659.

[35] Jog, C. S., 2015. *Continuum Mechanics*, Vol. 1. Cambridge University Press.

[36] Davis, S., and Caldwell, D. G., 2006. "Braid effects on contractile range and friction modeling in pneumatic muscle actuators". *The International Journal of Robotics Research,* **25**(4), pp. 359–369.

[37] Hocking, E. G., and Wereley, N. M., 2012. "Analysis of nonlinear elastic behavior in miniature pneumatic artificial muscles". *Smart Materials and Structures,* **22**(1), p. 014016.

[38] Simaan, N., Taylor, R., and Flint, P., 2004. "A dexterous system for laryngeal surgery". In IEEE Conference on Robotics and Automation, 2004, Vol. 1, pp. 351–357.

[39] Camarillo, D. B., Milne, C. F., Carlson, C. R., Zinn, M. R., and Salisbury, J. K., 2008. "Mechanics modeling of tendon-driven continuum manipulators". *IEEE Transactions on Robotics,* **24**(6), pp. 1262–1273.

[40] Kato, T., Okumura, I., Song, S.-E., Golby, A. J., and Hata, N., 2015. "Tendon-driven continuum robot for endoscopic surgery: Preclinical development and validation of a tension propagation model". *IEEE/ASME Transactions on Mechatronics,* **20**(5), pp. 2252–2263.

[41] Kuo, C.-H., Chen, Y.-C., and Pan, T.-Y., 2017. "Continuum kinematics of a planar dual-backbone robot based on pseudo-rigid-body model: formulation, accuracy, and efficiency". In ASME 2017 International Design Engineering Technical Conferences & Computers & Information in Engineering Conference, August 6-9, 2017, Cleveland, USA, pp. V05AT08A015–V05AT08A015.

[42] Shahabi, E., and Kuo, C.-H., 2018. "Solving inverse kinematics of a planar dual-backbone continuum robot using neural network". In European Conference on Mechanism Science, September 4-6, 2018, Aachen, Germany, pp. 355–361.

[43] Menon, M. S., Ananthasuresh, G., and Ghosal, A., 2013. "Natural motion of one-dimensional flexible objects using minimization approaches". *Mechanism and Machine Theory,* **67**, pp. 64–76.

[44] Ghosal, A., 2006. *Robotics: Fundamental Concepts and Analysis*. Oxford University Press.

[45] Hartley, R., and Zisserman, A., 2003. *Multiple View Geometry in Computer Vision*. Cambridge University Press.

[46] Carter, F., Frank, T., Davies, P., and Cuschieri, A., 2000. "Puncture forces of solid organ surfaces". *Surgical Endoscopy,* **14**(9), pp. 783–786.

[47] Artifon, E. L., Cheng, S., Nakadomari, T. T., Kashiwagi, L., Ardengh, J. C., Belmonte, E., and Otoch, J. P., 2018. "Ex vivos models to teaching therapeutic endoscopic ultrasound (t-eus)". *Revista de Gastroenterología del Perú,* **38**(1), pp. 103–110.

List of Figure Captions & Page numbers

List of Table Captions& Page numbers